Oxygen and silicon contents of Earth's core from high pressure metal–silicate partitioning experiments

Angele Ricolleau [a,b,*], Yingwei Fei [b], Alexandre Corgne [c], Julien Siebert [a,d], James Badro [a,d]

[a] Institut de Physique du Globe de Paris, Paris, France
[b] Geophysical Laboratory, Carnegie Institution of Washington, Washington DC, USA
[c] IRAP, Université de Toulouse, CNRS, Toulouse, France
[d] IMPMC, Université Pierre et Marie Curie, CNRS, Paris, France

ARTICLE INFO

ABSTRACT

Oxygen and silicon partitioning between molten metal and silicate melts was measured in samples synthesized in piston-cylinder and multi-anvil presses between 2 and 21 GPa, 2273 and 2873 K, and at oxygen fugacities of 1.5–3.6 log units below the iron–wüstite buffer. Our partitioning data are used together with published data to parameterize the individual effects of pressure, temperature and composition on the partitioning of oxygen and silicon. Results show that the oxygen metal–silicate partition coefficient increases with increasing oxygen fugacity, temperature and pressure, whereas the silicon metal-silicate partition coefficient increases with decreasing oxygen fugacity, increasing temperature and pressure. Silicon and oxygen contents of Earth's core were derived for different core formation models. Considering single-stage core formation at 40 GPa, 3200 K, IW-2, the core would contain 1 to 3.5 wt.% silicon and 0.5 to 2.5 wt.% oxygen. In a continuous core-formation scenario, and depending on the oxidation path, Si core content varies from 1 to 11 wt.%, whereas oxygen content ranges from 0 to 2.5 wt.%. These models show that the oxygen content in the core cannot be significantly higher than 2.5 wt.%. In these compositional models, a range of combined silicon and oxygen concentrations in the core could satisfies the seismologically observed range of outer core density deficits.

© 2011 Elsevier B.V. All rights reserved.

1. Introduction

The molten outer core density deficit (CDD) compared to pure iron at the same conditions was first estimated to be around 10% (Birch, 1952). More recently, Anderson and Isaak (2002) updated the value of the CDD between 2.9 and 7% depending on the temperature at the inner-outer core boundary (ICB). The CDD is accommodated by incorporating one or several light elements in the core, the amount of which varies depending on the light element(s) in question. The favoured candidates are silicon, sulphur, oxygen, hydrogen and carbon (e.g., Poirier, 1994). Geochemical and cosmochemical constraints impose less than 2 wt.% sulphur and about 0.2 wt.% carbon in the core (Dasgupta and Walker, 2008; Dreibus and Palme, 1996; McDonough, 2003). Because of limited interactions between the core and mantle since core formation (e.g., McDonough, 2003), the nature and concentration of the light element(s) are directly linked to metal–silicate partitioning of these elements during core-mantle differentiation. How the core came to its present configuration depends on the available material to make it, and the conditions

of its differentiation. Commonly, the bulk Earth's composition is considered similar to that of the CI chondrites composition corrected for volatile depletion, CI chondrites being primitive meteorites with a composition resembling that of the solar photosphere (e.g., Palme and Jones, 2003). Comparison of the siderophile element concentration in meteorites and in the Earth's mantle with experimental partitioning between molten metal and silicate melts provides an insight into the pressure and temperature conditions of core segregation (see for example the review by Righter, 2003). However, the conditions of core differentiation remain unclear and several models have been proposed in recent years. Most of these models consider that core formation took place through metal segregation in a deep silicate magma ocean, as a consequence of the large amount of heat available in early Earth's history. The simplest model, known as the single-stage model, considers that core materials equilibrated at the base of the magma ocean in a single event, namely at fixed conditions (e.g., Li and Agee, 1996; Righter et al., 1997). It has also been proposed that the single equilibration conditions may more plausibly represent an average of a wider range of conditions during a more dynamic process (Li and Agee, 1996). In agreement with dynamical models of Earth's accretion (Kaula, 1995; O'Brien et al., 2006), several studies have recently proposed that core formation occurred as a largely continuous process, with core segregation starting well before

the end of Earth's accretion and under progressively more oxidising conditions as the Earth grew (Galimov, 2005; O'Neill, 1991; Wade and Wood, 2005).

Silicon is currently seen as the most probable light element in the core. Recent sound velocity measurements carried out at high pressure on solid Fe-alloy and extrapolated to conditions of the inner core concluded that a few percent of Si was likely present in the bulk core (Antonangeli et al., 2010; Badro et al., 2007). Metal–silicate partitioning data, which reveal that Si becomes more siderophile at reduced conditions and high temperatures, also support the presence of Si in the core (e.g., Wade and Wood, 2005). Partitioning studies have not provided a consistent value for the amount of Si in the core, mainly because the pressure dependence of Si partition coefficient has remained controversial, with negative correlations derived in Mann et al. (2009) and Corgne et al. (2008) but positive correlations found in Wade and Wood (2005) and Gessmann et al. (2001).

Oxygen has also been put forward as a possible major light element in Earth's core based on sound velocity measurements on iron alloys (Badro et al., 2007) and on required element partitioning between inner and outer core to account for seismic measurements (Alfè et al., 2002). At present, there is no systematic study of the partitioning of oxygen between metal and silicate melts. With the exception of the study of Li and Agee (2001), who explored a large range of metal and silicate compositions to study the behaviour of sulphur, silicon and oxygen, partition coefficients for oxygen have only been measured between molten metal and mantle minerals (ferropericlase or perovskite) and used as proxy for molten metal–molten silicate partitioning (Asahara et al., 2007; Frost et al., 2010; Kawazoe and Ohtani, 2006; O'Neill et al., 1998; Ozawa et al., 2008; Rubie et al., 2004; Takafuji et al., 2005). All these studies agree on a significant increase of oxygen solubility with temperature. Early studies concluded that pressure has a negative effect on the solubility of oxygen in metal (Li and Agee, 2001; O'Neill et al., 1998; Rubie et al., 2004). However, more recent studies suggested the existence of two pressure regimes, with a decrease of oxygen concentration in the metal up to 10 GPa and subsequently a moderate increase at higher pressures (Asahara et al., 2007; Frost et al., 2010). Overall, these studies suggest that the effect of pressure remains moderate in comparison to that of temperature.

As first mentioned by Birch (1964), the core density deficit could be accounted for by a combination of several light elements, rather than just one. Thus, it is important to understand the interactions between proposed light elements during core formation. Silicon and oxygen are major elements in the bulk Earth, and were readily available in large quantities during all stages of terrestrial accretion. It is therefore fundamental to study their partitioning between molten metal and silicate melts at pressure, temperature and redox conditions relevant to core formation. To date, the coupled behaviour and solubility of silicon and oxygen in molten metal have only been studied in association with a single crystallised mineral phase, perovskite, whereas realistic conditions of core-mantle differentiation in a magma ocean are that of a molten silicate with peridotitic composition. Available solubility data (Ozawa et al., 2009; Sakai et al., 2006; Takafuji et al., 2005) suggest that silicon and oxygen could be the main light elements, but uncertainties regarding equilibrium and oxygen fugacity (fO_2) conditions in these extremely high-pressure experiments prevent the drawing of definitive conclusions. In order to constrain better the Si and O contents of the Earth's core, we need to measure their partition coefficients between molten metal and molten silicate as a function of composition, P, T, fO_2 conditions, since core formation probably happened continuously, with changing metal-silicate equilibration depths, temperatures, and redox conditions (e.g., Corgne et al., 2008; Wade and Wood, 2005).

The objective of this experimental study was to derive partition coefficients for oxygen and silicon at conditions that prevailed during core formation in a primordial magma ocean. High-pressure high-temperature melting experiments were performed to collect the required data, which were integrated in a thermodynamic model to parameterize partitioning and chemical interactions as a function of key variables. Our data are used to answer ambiguities emerging from previous studies and to derive plausible ranges of Si and O contents in the core for proposed core formation models.

2. Methods

2.1. Experimental procedure

Melting and equilibration experiments were performed using two synthetic compositions prepared from high purity powders of oxides and iron metal. The first starting material (SM1) is a 1:1 mixture (weight ratio) of pure iron metal and an $MgSiO_3$ composition prepared by mixing MgO with SiO_2. The second starting material (SM2) is a mixture (1:1 weight ratio) of pure iron metal and oxides (MgO, Fe_2O_3 and SiO_2 in 0.70:0.15:1 relative molar proportions). The starting powders were pre-homogenised under ethanol and stored in an oven at 100 °C.

Melting experiments were carried out between 2273 and 2873 K and 2 and 21 GPa, using an end-loaded piston-cylinder apparatus and a 1500-ton multi-anvil press at the Geophysical Laboratory. In all runs, starting mixtures were contained in MgO capsules prepared from polycrystalline magnesia rods. For experiments performed at 2 GPa and 2273 K, we used a graphite furnace surrounded by a Pyrex glass and talc as pressure medium. For experiments at 2573 K and 2873 K, we used a piston-cylinder cell assembly similar to the one described in Cottrell and Walker (2006) with $LaCrO_3$ as thermal insulator. For experiments at 7 GPa and 2273 K, we used the 18/11 assembly as described in Corgne et al. (2007). For experiments at 2573 K and 2873 K, we used the same 18/11 assembly but the outer zirconia sleeve was replaced by a thicker $LaCrO_3$ sleeve for better thermal insulation. For experiments at 14 GPa and 21 GPa, we used the 10/5 and 8/3 assemblies respectively, as described by Bertka and Fei (1997).

Temperatures in all experiments were measured using a W5%Re/ W26%Re thermocouple placed directly above the MgO capsule. The samples were heated at a rate of 100 K/min to the target temperature, held there for 2 min and quenched by turning off the power to the furnace. Run duration of 2 min ensured approach of equilibrium at such high temperatures (as evidenced from flat chemical profiles across the run products; see Fig. S2), while limiting interaction of the sample with the MgO capsule. Runs showing W or Re contamination of the metallic phase were discarded and redone.

Retrieved samples were mounted in epoxy resin and carefully polished using a suite of diamond powder grit from 150 μm to 0.25 μm to avoid SiC contamination. Polishing using regular SiC sheets and an alumina suspension was observed to lead to significant implantation of Si-rich particles in the metallic phase.

2.2. Analytical procedure

Chemical analyses were performed on carbon-coated samples with a JEOL 8900 electron microprobe at the Geophysical Laboratory using a 15 kV acceleration voltage and a 30 nA probe current. Standards used for analysis of the metallic phase were pure Fe metal, pure Si metal and magnetite (Fe_3O_4) for Fe, Si and O, respectively; for analysis of molten silicate and ferropericlase, standards were enstatite for Si, Mg and O, and magnetite for Fe. When analysing O in the metal phase, we applied a background correction determined from pure iron standard measurement before and after each unknown. The magnitude of the correction was 0.15 wt% $\pm$ 0.02 (1sd). Microprobe analyses of the silicate melts were performed using a scan window of 10×10 μm to average the heterogeneous quench texture. As done in previous studies (Gessmann and Rubie, 1998; O'Neill et al., 1998), we used image analysis to obtain the bulk composition of the molten metal (prior to quench), which integrates the individual

compositions of the quenched metal alloy and exsolved blobs (upon quenching) using their respective proportion. We also used another approach, which consisted in bulk analyses of the entire blob-bearing metal phase with a 10×10 μm scan mode. The two methods produced consistent results. Because exsolved blobs were too small for analysis in some runs, the second method proved to be more appropriate overall. Metal contents discussed hereafter are therefore the ones obtained with the second approach.

3. Results

3.1. Samples textures and compositions

Fig. 1 shows typical quench textures. As expected from previous works using a similar experimental approach, (Mg,Fe)O ferroperi-clase grains formed from the reaction between the MgO capsule and the starting composition (Fig. 1a). Such contamination is inherent to these experiments using MgO capsule and cannot be avoided (e.g., Kegler et al., 2008; Li and Agee, 2001; Righter et al., 2010). By limiting the duration of the runs it is possible to keep a significant fraction of the silicate melt in equilibrium with the metal. This melt is enriched in MgO in similar proportions for the various runs of this work. The MgO-rich silicate melt quenched as a fine matrix of quench crystals and glass. The metallic alloys adopted two different textures depending on run pressure. In all runs, O-rich blobs were observed as inclusions in the metal phase (Fig. 1b-c), with the exception of a 10–20 μm border zone. As previously discussed (Gessmann and Rubie, 1998; O'Neill et al., 1998), these blobs have formed by exsolution from an initially homogeneous molten alloy upon temperature quenching. Quench rates being larger for runs performed at 14–21 GPa, the size distribution of blobs in these runs relative to runs at 2–7 GPa is cha-racterised by a larger number of smaller blobs (Fig. 1c).

Chemical compositions of molten silicate, ferropericlase and mol-ten metal are presented in Table 1. The produced silicate melts con-tains 27–37 wt.% Mg, 17–24 wt.% Si and between 1 and 15 wt.% Fe, that is to say a composition approximating that of an olivine solid so-lution. The metallic phase consists almost entirely of Fe (>97 wt.% Fe) with minor amounts of O and Si. Exsolved blobs large enough to be analysed (in spot mode) show a composition close to pure FeO in runs using SM2 and contain Fe, O and some Si in runs using SM1. Ox-ygen concentrations in the metal were obtained from all 25 runs, whereas silicon concentrations were measured in only 11 samples, for which concentrations were above microprobe detection limits (~500 ppm). The oxygen content of the metal increases slightly with pressure (Fig. 2a). As previously reported by Rubie et al. (2004) and Asahara et al. (2007), the oxygen content in the metal phase also increases with increasing oxygen fugacity and increasing temperature (Fig. 2b). The silicon content of the metal increases slightly with increasing pressure (Fig. 2c).

3.2. Oxygen fugacity and activity coefficients

In order to derive a thermodynamic model for oxygen and silicon partitioning between metal and silicate, we first need to determine the oxygen fugacity of each run. Oxygen fugacity (ΔIW) is determined relative to the iron–wüstite buffer:

$$\Delta \text{IW} = 2 \log \frac{a_{\text{FeO}}^{\text{sil}}}{a_{\text{Fe}}^{\text{met}}} = 2 \log \frac{x_{\text{FeO}}^{\text{sil}}}{x_{\text{Fe}}^{\text{met}}} + 2 \log \frac{\gamma_{\text{FeO}}^{\text{sil}}}{\gamma_{\text{Fe}}^{\text{met}}} \tag{1}$$

where the activity coefficient (γ) of component M (Fe or FeO) in a phase (met: metal or sil: silicate) is the ratio of the activity (a) to the mole fraction (x) according to the relation:

$$a_M^{phase} = \gamma_M^{phase} \cdot x_M^{phase} \tag{2}$$

In the metal, the activity coefficient of the solvent Fe (γ_{Fe}) is calcu-lated using the formalism described in Ma (2001) as:

$$
\begin{aligned}
\ln \gamma_{\text{Fe}}^{\text{met}} = & \sum_{i=2}^{N} \varepsilon_i^i (x_i + \ln(1 - x_i)) \\
& - \sum_{j=2}^{N-1} \sum_{k=j+1}^{N} \varepsilon_j^k x_j x_k \left(1 + \frac{\ln(1 - x_j)}{x_j} + \frac{\ln(1 - x_k)}{x_k} \right) \\
& + \sum_{i=2}^{N} \sum_{\substack{k=2 \\ (k \neq i)}}^{N} \varepsilon_i^k x_i x_k \left(1 + \frac{\ln(1 - x_k)}{x_k} - \frac{1}{1 - x_i} \right) \\
& + \frac{1}{2} \sum_{j=2}^{N-1} \sum_{k=j+1}^{N} \varepsilon_j^k x_j^2 x_k^2 \left(\frac{1}{1 - x_j} + \frac{1}{1 - x_k} - 1 \right) \\
& - \sum_{i=2}^{N} \sum_{\substack{k=2 \\ (k \neq i)}}^{N} \varepsilon_i^k x_i^2 x_k^2 \left(\frac{1}{1 - x_i} + \frac{1}{1 - x_k} + \frac{x_i}{2(1 - x_i)^2} - 1 \right)
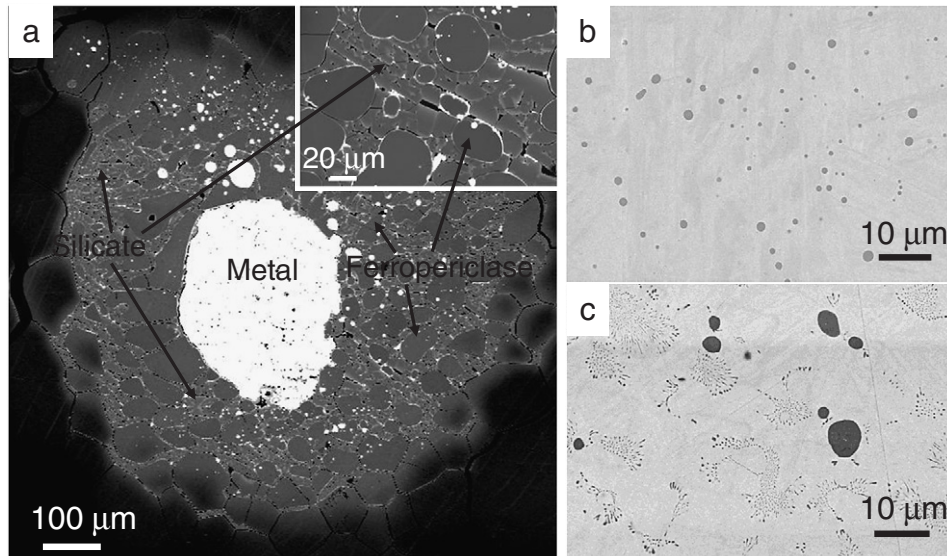\end{aligned} \tag{3}
$$

Fig. 1. Backscattered electron images of quenched samples. a) Sample synthesized at 7 GPa and 2573 K (run PR824). On the top right is a magnification of the quench silicate sur-rounded by ferropericlase grains. b) Example of FeO blobs present in the quenched molten metal in samples synthesized at 2 GPa and 2273 K (run PC799). c) Example of mixed quench texture observed in samples synthesized at pressure of 14 GPa and 21 GPa (run M1107).

Table 1
Experimental conditions, average compositions (in wt.%) of the molten metal, silicate melt and coexisting ferropericlase grains present in highest temperature runs. Numbers in parentheses are uncertainties given as two standard deviations of the respective population.

Run	P (GPa)	T (K)	SM	nbo/t	ΔIW[a1]	ΔIW[a2]	ΔIW[a3]	Phase (n)	Si (wt.%)	O (wt.%)	Fe (wt.%)	Mg (wt.%)	Total
PC797	2	2273	SM1	4.22	−3.16	−2.33		met (112)	0.09 (1)	0.06 (2)	101.21 (7)	–	101.51
								sil (61)	19.18 (12)	45.77 (25)	3.07 (46)	33.69 (25)	101.71
PC855	2	2573	SM1	4.17	−4.21	−3.46	−3.27	met (20)	0.46 (1)	0.01 (1)	99.21 (11)	–	99.68
								sil (13)	19.74 (61)	44.49 (76)	0.94 (10)	35.18 (1.05)	100.36
								Fp (15)		38.52 (15)	1.92 (08)	59.90 (07)	100.35
PC772	2	2873	SM1	4.62	−4.21	−3.61	−3.29	met (100)	0.94 (6)	0.10 (7)	99.13 (19)	–	100.36
								sil (14)	18.64 (1.29)	45.22 (73)	0.94 (12)	36.82 (1.77)	101.63
								Fp (56)		40.65 (19)	1.96 (07)	60.29 (16)	102.92
PR682	7	2273	SM1	4.74	−3.30	−2.51		met (124)	0.66 (9)	0.12 (7)	99.23 (33)	–	100.17
								sil (40)	18.02 (1.57)	44.89 (46)	2.65 (27)	35.87 (2.05)	101.42
PR814	7	2573	SM1	4.11	−3.10	−2.39		met (132)	0.35 (8)	0.14 (6)	99.29 (22)	–	99.94
								sil (40)	19.48 (12)	45.19 (22)	3.29 (17)	33.25 (21)	101.21
PR825	7	2873	SM1	4.63	−2.69	−2.18	−2.47	met (151)	0.08 (6)	0.22 (6)	98.61 (20)	–	99.07
								sil (35)	18.23 (74)	45.28 (43)	5.31 (85)	34.17 (57)	102.98
								Fp (10)		40.91 (17)	5.09 (13)	58.37 (18)	104.39
PR741	7	2873	SM1	4.19	−3.07	−2.47	−2.84	met (100)	0.37 (8)	0.16 (7)	98.41 (20)	–	99.12
								sil (24)	19.19 (46)	44.88 (49)	3.41 (40)	33.30 (60)	100.78
								Fp (16)		40.73 (12)	3.29 (38)	59.57 (19)	103.62
M1112	14	2573	SM1	3.30	−2.84	−2.05	−2.17	met (174)	1.00 (19)	0.49 (15)	96.75 (34)	–	98.40
								sil (35)	21.44 (71)	44.29 (36)	4.11 (58)	28.94 (1.35)	98.78
								Fp (11)		39.16 (29)	6.22 (73)	55.70 (53)	101.11
M1123	14	2873	SM1	3.70	−3.03	−2.38	−2.46	met (99)	1.56 (09)	0.34 (8)	98.25 (20)	–	100.31
								sil (14)	19.02 (2.92)	44.17 (1.00)	3.03 (74)	33.19 (4.13)	99.41
								Fp (29)		39.79 (19)	4.78 (37)	58.15 (28)	102.75
LO722	21	2573	SM1	2.77	−3.06	−2.17	−2.22	met (73)	1.22 (8)	0.21 (7)	99.50 (27)	–	101.08
								sil (27)	24.04 (80)	44.89 (60)	3.24 (40)	27.37 (1.05)	99.54
								Fp (24)		39.67 (24)	5.85 (1.15)	57.87 (68)	103.42
LO728	21	2873	SM1	2.86	−2.46	−1.76	−2.18	met (99)	0.96 (14)	0.44 (13)	99.21 (35)	–	100.77
								sil (32)	24.33 (1.45)	45.02 (86)	6.51 (2.06)	27.28 (2.04)	103.13
								Fp (16)		39.41 (64)	6.45 (1.49)	57.22 (1.46)	103.52
PC799	2	2273	SM2	4.87	−1.75	−1.22		met (116)	–	0.56 (11)	100.78 (12)	–	101.50
								sil (58)	17.02 (54)	42.26 (76)	14.66 (2.31)	29.28 (92)	103.21
PC848	2	2273	SM2	4.68	−1.73	−1.19		met (155)	–	0.47 (17)	99.20 (32)	–	99.96
								sil (61)	17.73 (55)	42.23 (81)	15.14 (2.24)	29.09 (1.02)	104.19
PC842	2	2573	SM2	4.14	−2.91	−2.22		met (250)	–	0.14 (2)	100.03 (13)	–	100.33
								sil (21)	19.69 (14)	45.06 (28)	4.20 (38)	33.48 (24)	102.43
PC854	2	2573	SM2	4.08	−3.11	−2.40	−2.55	met (61)	-	0.12 (2)	99.47 (31)	–	99.76
								sil (32)	19.59 (14)	44.18 (61)	3.27 (26)	33.18 (38)	100.23
								Fp (10)		40.17 (20)	4.53 (14)	59.03 (14)	103.74
PC801	2	2873	SM2	4.35	−2.78	−2.22	−2.68	met (264)	–	0.38 (16)	99.27 (31)	–	99.93
								sil (12)	18.96 (37)	41.47 (68)	4.80 (1.17)	33.58 (60)	98.81
								Fp (12)		36.40 (23)	4.01 (15)	58.56 (21)	98.98
PR683	7	2273	SM2	4.33	−2.20	−1.50		met (94)	–	0.58 (13)	100.00 (20)	–	100.85
								sil (48)	18.48 (22)	43.49 (40)	8.98 (97)	30.69 (45)	101.64
PR805	7	2573	SM2	4.71	−2.29	−1.73	−1.96	met (184)	–	0.28 (9)	98.58 (49)	–	99.10
								sil (43)	17.47 (71)	42.81 (47)	8.23 (81)	31.95 (63)	100.46
								Fp (5)		39.07 (15)	8.69 (06)	55.24 (22)	103.02
PR824	7	2573	SM2	4.21	−2.44	−1.82	−1.93	met (135)	–	0.45 (15)	97.27 (59)	–	98.07
								sil (35)	18.65 (17)	43.78 (42)	6.75 (47)	30.99 (27)	100.17
								Fp (10)		39.43 (20)	8.91 (47)	55.16 (36)	103.52
PR740	7	2873	SM2	4.13	−2.68	−2.12	−2.42	met (100)	–	0.59 (14)	99.08 (18)	–	99.89
								sil (47)	19.05 (11)	47.37 (19)	5.19 (31)	31.83 (22)	103.45
								Fp (16)		42.28 (21)	5.25 (59)	57.21 (35)	104.76
M1107	14	2573	SM2	4.04	−1.96	−1.42	−1.45	met (84)	–	0.84 (14)	99.19 (16)	–	100.20
								sil (35)	18.54 (15)	43.31 (37)	12.21 (1.12)	27.48 (67)	101.54
								Fp (6)		37.82 (37)	14.92 (73)	49.39 (60)	102.22
M1122	14	2873	SM2	3.34	−3.14	−2.44	−1.95	met (168)	–	0.58 (9)	99.37 (30)	–	100.24
								sil (20)	22.02 (69)	45.91 (57)	3.08 (35)	30.50 (1.08)	101.51
								Fp (36)		38.84 (38)	8.80 (1.15)	55.30 (87)	102.98
LO719	21	2573	SM2	3.13	−2.24	−1.52	−1.35	met(232)	–	1.09 (19)	98.85 (19)	–	100.14
								sil (43)	21.82 (95)	44.36 (43)	8.05 (1.38)	26.06 (1.14)	100.28
								Fp (21)		37.54 (1.03)	15.77 (4.13)	49.37 (3.06)	102.72
LO730	21	2873	SM2	2.93	−2.25	−1.60	−1.71	met (14)	–	0.47 (11)	98.97 (19)	–	99.62
								sil (19)	23.39 (1.92)	45.50 (62)	8.47 (48)	25.89 (2.43)	103.24
								Fp (29)		38.81 (64)	11.24 (2.74)	53.31 (1.87)	103.38
LO734	21	2873	SM2	4.46	−1.92	−1.53	−1.74	met (110)	–	0.74 (17)	98.90 (25)	–	99.90
								sil (28)	18.28 (1.27)	42.93 (1.51)	11.32 (4.98)	30.07 (2.90)	102.59
								Fp (28)		39.32 (89)	10.46 (3.35)	53.09 (2.87)	103.66

All melting experiments were performed in MgO capsules and equilibrated during 2 min at the target temperature. P: pressure, T: temperature, n: number of electron probe analyses, met: metal, sil: silicate, and Fp: ferropericlase. [a] ΔIW corresponds to the logarithm of the oxygen fugacity relative to the iron–wüstite (IW) buffer; [a1] calculated assuming an ideal mixing behaviour; [a2] calculated using the activity coefficient for each species; [a3] calculated using the FeO content in ferropericlase surrounding the metal and silicate melts and using the activity coefficient of FeO given by Frost (2003).
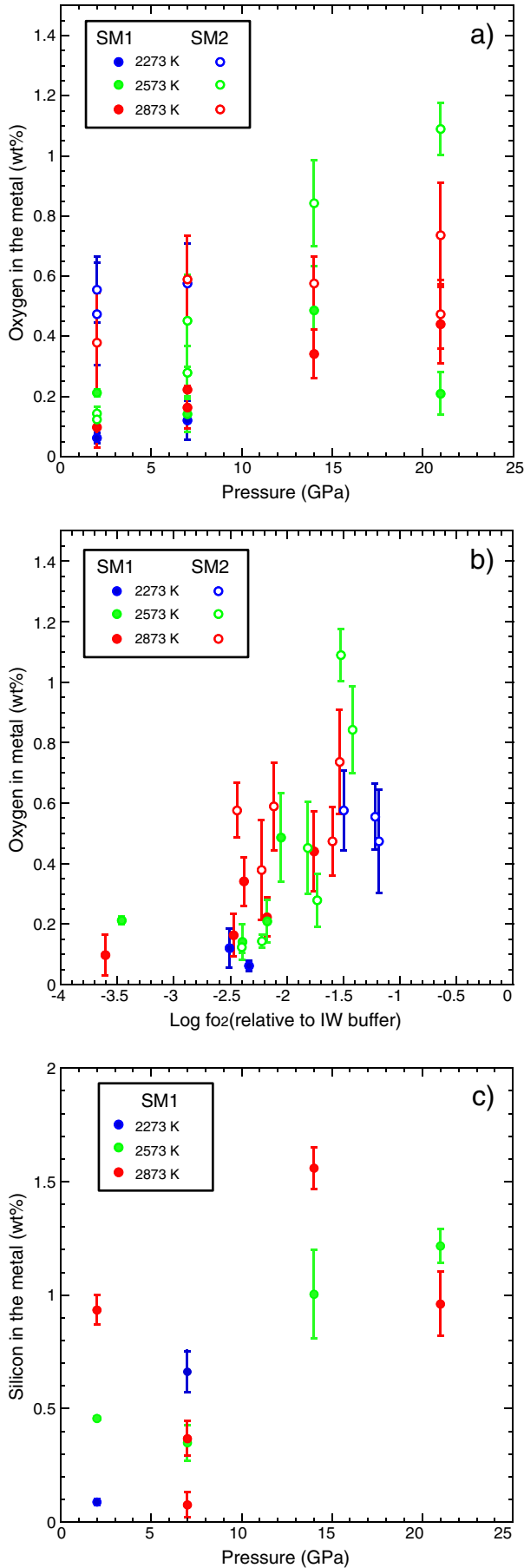
where x_i is the molar fraction of the solute i infinitely dilute in pure iron, N is the number of solutes in molten Fe. The interaction parameters ε_i^j describe the measured effects of component i on the activity coefficient of component j and $\varepsilon_i^j = \varepsilon_j^i$. These parameters are equivalent to Margules interaction parameters used in other formalisms. For the Fe–Si–O ternary system (our data), Eq. (3) can be simplified to:

$$\ln \gamma_{Fe}^{met} = \varepsilon_{Si}^{Si}(x_{Si} + \ln(1-x_{Si})) + \varepsilon_O^O(x_O + \ln(1-x_O))$$
$$+ \varepsilon_{Si}^O x_{Si} x_O \left(1 - \frac{1}{1-x_{Si}} - \frac{1}{1-x_O}\right) \qquad (4)$$
$$- \frac{1}{2}\varepsilon_{Si}^O x_{Si}^2 x_O^2 \left(\frac{3}{1-x_{Si}} + \frac{3}{1-x_O} + \frac{x_{Si}}{(1-x_{Si})^2} + \frac{x_O}{(1-x_O)^2} - 3\right).$$

For silicon, we used ε_{Si}^{Si} from Dresler (1989) where:

$$\varepsilon_{Si}^{Si} = 7.039 + 7898/T. \qquad (5)$$

For oxygen, we used $\varepsilon_O^O = -10.5$ from the Steelmaking Data Sourcebook (1988) and $\varepsilon_O^{Si} = \varepsilon_{Si}^O = 12.9$ from Shibaev and Grigorovich (2008), which are the values obtained at the reference temperature of 1873 K (T^0). We then used the equation given in the Steelmaking Data Sourcebook (1988) to extrapolate the values at our experimental temperatures:

$$\varepsilon_i^j(T) = \frac{T^0}{T}\varepsilon_i^j\left(T^0\right). \qquad (6)$$

In the silicate, the activity coefficient (γ) of FeO was obtained by using the equation given in Basu et al. (2008):

$$\ln \gamma_{FeO}^{sil} = 2906/T - 2.6024\, X(FeO) + 2.2105\, X(SiO_2) - 0.9666. \qquad (7)$$

Another method to calculate the oxygen fugacity in experimental runs is to use the measured content of FeO in ferropericlase to obtain the oxygen fugacity. By using the equation of Frost (2003) for the activity coefficient of FeO in ferropericlase, we obtained values of oxygen fugacity close to the values obtained using the silicate melts as shown in Table 1. The difference in the calculated oxygen fugacity between the two methods is less than 0.5 log unit.

3.3. Oxygen partitioning

The exchange reaction of oxygen between silicate and metal liquids can be written as:

$$FeO(sil) = Fe(met) + O(met) \qquad (8)$$

The equilibrium constant for the reaction is defined as:

$$K_O = \frac{a_{Fe}^{met}\, a_O^{met}}{a_{FeO}^{sil}} \qquad (9)$$

where a_{Fe}^{met}, a_O^{met} and a_{FeO}^{sil} are the activities of iron and oxygen in the molten metal, and the activity of FeO in the silicate melt, respectively. Taking the logarithm, we derive the following relationship between K_O and oxygen fugacity:

$$\log K_O = \log a_O^{met} - \Delta IW/2. \qquad (10)$$

Fig. 2. Oxygen content measured in the metal as a function of pressure (a), and oxygen fugacity relative to the iron–wüstite buffer (b) (ΔIW calculated using the activity coefficient for each species). c) Silicon content measured in the metal as a function of pressure.

Rearranging Eq. (9) using Eq. (2) gives:

$$\log K_O = \log \frac{x_{Fe}^{met} x_O^{met}}{x_{FeO}^{sil}} + \log \frac{\gamma_{Fe}^{met} \gamma_O^{met}}{\gamma_{FeO}^{sil}} = \log K_{exp} + \log \frac{\gamma_{Fe}^{met} \gamma_O^{met}}{\gamma_{FeO}^{sil}} \quad (11)$$

where K_{exp} is the ratio of mole fraction of Fe and O in metal over FeO in silicate, which is obtained from chemical analyses of our experimental runs. The activity coefficients γ_{Fe}^{met} and γ_{FeO}^{sil} are calculated with Eqs. (4) and (7), respectively.

To estimate the activity coefficient of oxygen, we used the formalistic description given by Shibaev et al. (2005) that takes account of the O–Si and O–Fe interactions explicitly:

$$\ln \gamma_{O(Fe)}^0 = 4.29 - 16500/T \quad (12)$$

and

$$\ln \gamma_{O(Si)}^0 = 15.18 - 46265/T \quad (13)$$

where $\gamma_{O(Fe)}^0$ and $\gamma_{O(Si)}^0$ are the activity coefficients of oxygen at infinite dilution in pure liquid iron and silicon, respectively. Then, the activity coefficient of oxygen in Fe–Si melt, $\gamma_{O(Fe-Si)}^0$, is given by:

$$\ln \gamma_{O(Fe-Si)}^0 = x_{Fe} \ln \gamma_{O(Fe)}^0 + x_{Si} \ln \gamma_{O(Si)}^0$$
$$+ x_{Si} x_{Fe} \left\{ x_{Fe} \left(\ln \frac{\gamma_{O(Fe)}^0}{\gamma_{O(Si)}^0} + \varepsilon_{O(Fe)}^{Si} \right) + x_{Si} \left(\ln \frac{\gamma_{O(Si)}^0}{\gamma_{O(Fe)}^0} + \varepsilon_{O(Si)}^{Fe} \right) \right\} \quad (14)$$

where the interaction parameters $\varepsilon_{O(Fe)}^{Si} = 12.5$ and $\varepsilon_{O(Si)}^{Fe} = -6.5$ at 1873 K (Shibaev et al., 2005; Shibaev and Grigorovich, 2008). We used Eq. (6) to calculate them at higher temperature. Like Shibaev et al. (2005), we neglected the effect of oxygen on its own activity coefficient due to the low solubility of oxygen in the liquid alloy and assumed that γ_O^0 is equal to γ_O.

The equilibrium constant of the exchange reaction is related to the Gibbs free energy of formation, ΔG^0 from pure oxides and metals by:

$$RT\ln K_O = -\Delta G^0 = -\Delta H^0 + T\Delta S^0 - \int_{P^*}^{P} \Delta V \cdot dP \quad (15)$$

where R is the gas constant, ΔH^0 and ΔS^0 are the standard state enthalpy and entropy changes, and ΔV is the molar volume change of the exchange reaction.

By assuming a constant volume change, the equilibrium constant can be expressed as:

$$\log K_O = a + \frac{b}{T} + \frac{c \times P}{T} \quad (16)$$

where a, b and c are constants, T the temperature in Kelvin and P the pressure in GPa. In the absence of reliable equation of states for the studied components (molten silicate and Fe–Si–O), it is at this time difficult to assess variations in volume. For that reason, we assumed this term to be constant as done in previous partitioning studies (i.e. Righter et al., 1997; Wade and Wood, 2005). With this assumption, any dependence of the volume term to pressure is then empirically integrated in the pressure term (c) of Eq. (16). Comparing Eq. (15) and Eq. (16), it appears that the coefficients a and b are directly proportional to ΔS^0 and ΔH^0, respectively.

We used multivariate regression analysis to obtain the parameters a, b and c by fitting the Eq. (16) to the measured values of log K_O (n = 25). We derived the following parameterisation (uncertainties as ±1sd):

$$\text{Log } K_O = 2.19(\pm 0.53) - 10731(\pm 1329)/T + 33(\pm 18)P/T. \quad (17)$$
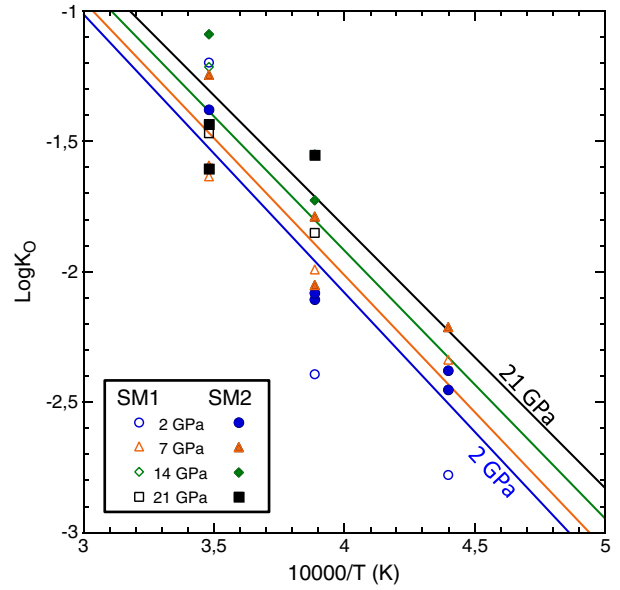

Fig. 3. The exchange coefficient log (K_O) for oxygen between molten metal and silicate melt as a function of inverse temperature (10,000/T). Lines are fits to the thermodynamic model (Eq. 17). Blue: 2 GPa, Orange: 7 GPa, Green: 14 GPa, Black: 21 GPa. Error on log (K_O) is 0.1 or below.

Using an exchange reaction rather than pure partitioning reaction, the effect of oxygen fugacity is intrinsically taken into account, indeed log K_O is a function of fO_2 and activity of oxygen in the metal (see Eq. (10) above and Figure S2). Fig. 3 shows the variation of log K_O for our data as a function of temperature and pressure, along with thermodynamic model fits. Oxygen partitioning in iron increases with both pressure and temperature, albeit the latter has a stronger effect.

3.4. Silicon partitioning

Similarly, the reaction that describes silicon exchange between metal and silicate can be expressed as:

$$2Fe(met) + SiO_2(sil) = 2FeO(sil) + Si(met) \quad (18)$$

The equilibrium constant for the reaction is defined as:

$$K_{Si} = \frac{\left(a_{FeO}^{sil}\right)^2 \left(a_{Si}^{met}\right)}{\left(a_{Fe}^{met}\right)^2 \left(a_{SiO_2}^{sil}\right)}. \quad (19)$$

Taking the logarithm and rearranging using molar fractions x and activity coefficients γ yields:

$$\log K_{Si} = \log \frac{\left(x_{FeO}^{sil}\right)^2 \left(x_{Si}^{met}\right)}{\left(x_{Fe}^{met}\right)^2 \left(x_{SiO_2}^{sil}\right)} + \log \frac{\left(\gamma_{Si}^{met}\right)}{\left(\gamma_{Fe}^{met}\right)^2} + \log \frac{\left(\gamma_{FeO}^{sil}\right)^2}{\left(\gamma_{SiO_2}^{sil}\right)}. \quad (20)$$

We obtained γ_{Fe}^{met} as described above (Eq. (3) for literature data and Eq. (4) for our data).

The activity coefficients of a solute in the alloy were obtained using the formalism described in Ma (2001) as:

$$\ln \gamma_i^{met} = \ln \gamma_{Fe} + \ln \gamma_i^0 - \varepsilon_i^i \ln(1-x_i) - \sum_{\substack{k=2 \\ (k \neq i)}}^{N} \varepsilon_i^k x_k \left(1 + \frac{\ln(1-x_k)}{x_k} - \frac{1}{1-x_i}\right)$$
$$+ \sum_{\substack{k=2 \\ (k \neq i)}}^{N} \varepsilon_i^k x_k^2 x_i \left(\frac{1}{1-x_i} + \frac{1}{1-x_k} + \frac{x_i}{2(1-x_i)^2} - 1\right). \tag{21}$$

This equation is simplified in a ternary system to:

$$\ln \gamma_i^{met} = \ln \gamma_{Fe} + \ln \gamma_i^0 - \varepsilon_i^i \ln(1-x_i) - \varepsilon_i^k x_k \left(1 + \frac{\ln(1-x_k)}{x_k} - \frac{1}{1-x_i}\right)$$
$$+ \varepsilon_i^k x_k^2 x_i \left(\frac{1}{1-x_i} + \frac{1}{1-x_k} + \frac{x_i}{2(1-x_i)^2} - 1\right). \tag{22}$$

In order to obtain the best parameterisation, we used additional experimental partitioning data from the literature (Corgne et al., 2008; Gessmann and rubie, 1998; Ito et al., 1995; Kilburn and Wood, 1997; Malavergne et al., 2007; Mann et al., 2009; Wade and Wood, 2001; Wade and Wood, 2005). The previously published data were corrected for the interaction with other siderophile elements present in those runs, sometimes up to 14 solutes, by using the general Eqs. (3) and (21). We used ε_{Si}^{Si} from Eq. (5) and γ_{Si}^0 from Dresler (1989) where:

$$\ln \gamma_{Si}^0 = 2.93 - 17014/T. \tag{23}$$

For the other solutes, interaction parameters ε_i^j were taken from the Steelmaking Data Sourcebook (1988). Most of the ε_i^j parameters were obtained at the reference temperature of 1873 K (T^0), we used the Eq. (7) to extrapolate the values to the relevant experimental temperatures. Values of the different parameters calculated for our experimental conditions are reported in Table S1.

To determine the relative contributions of pressure, temperature, and composition to the equilibrium constant, it can be expressed as a function of these variables using a slightly different analytical form as the used for O partitioning (Eq. 16):

$$\log K_{Si} = a + \frac{b}{T} + \frac{c \times P}{T} + d \times \text{nbo}/t \tag{24}$$

where a, b, c, and d are regression constants, T, the temperature in Kelvin, P, the pressure in GPa and nbo/t, the molar ratio of non-bridging oxygen per tetrahedrally coordinated cations in the silicate melt. Eq. (24) is similar to Eq. (16) except for the nbo/t term, which is an approximation of the ratio of activity coefficients of oxides in silicate melts (last term of Eq. 20). This ratio is poorly known and can be empirically fitted to the degree of polymerisation of a silicate melt as the nbo/t parameter (Mysen, 1988). Walter and Thibault (1995), Hillgren et al. (1996) and Jana and Walker (1997) have shown significant influence of silicate melt composition on the partitioning of siderophile elements. Although this parameter is intended to describe silica-saturated silicate melts (nbo/t<4), we also used it for our samples where the melt is ultrabasic (nbo/t>4). Note that we did not consider the nbo/t parameter to parameterize the oxygen exchange factor K_O because it only depends on the activity of FeO, for which we used the equation of Basu et al. (2008) (see Eq. (7)).

Multivariate regression of the experimental data (n = 75) leads to the following parameterisation for Si (uncertainties as ± 1sd):

$$\text{Log } K_{Si} = -1.12(\pm 0.62) - 11719(\pm 1177)/T$$
$$+ 100(\pm 22)P/T - 0.24(\pm 0.06)\text{nbo}/t \tag{25}$$

The variation of K_{Si} with temperature and pressure is shown in Fig. 4a, with symbols representing the experimental data (from this
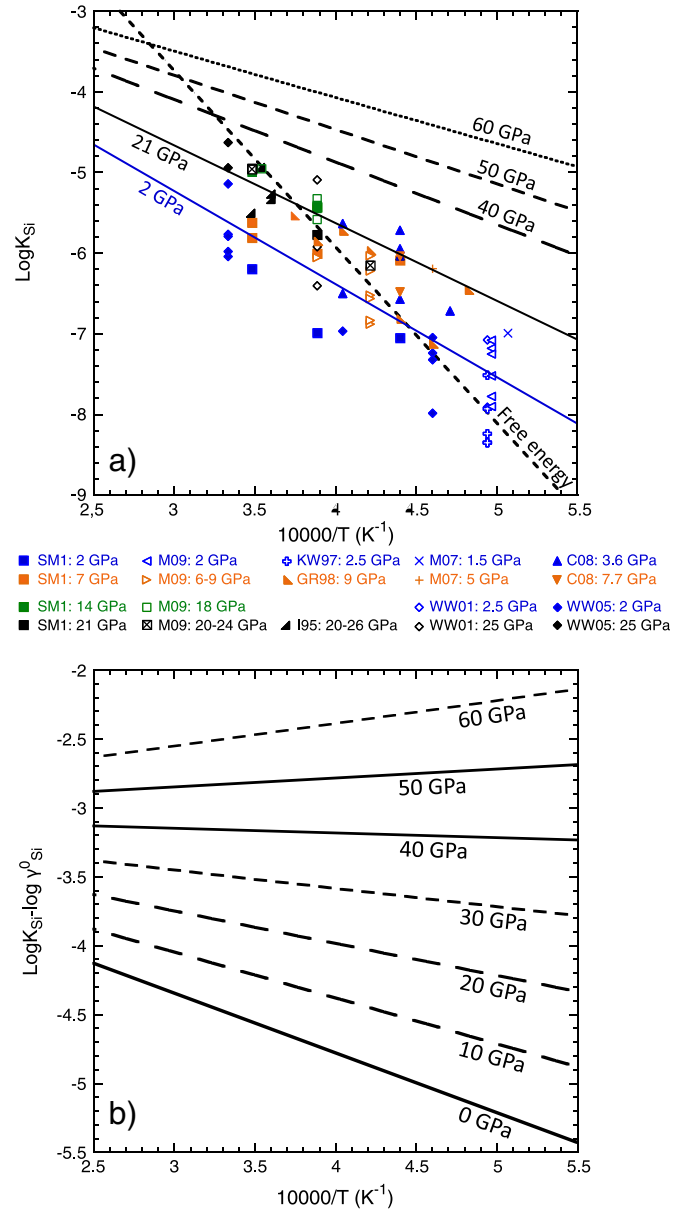

Fig. 4. a) The exchange coefficient log (K_{Si}) for silicon between molten metal and silicate melt as a function of inverse temperature (10,000/T). Our data (plain squares) and data from the literature are used for the regression. M09: Mann et al. (2009); KW97: Kilburn and Wood (1997); GR98: Gessmann and rubie (1998); I95: Ito et al. (1995); M07: Malavergne et al. (2007); WW01: Wade and Wood (2001); C08: Corgne et al. (2008); WW05: Wade and Wood (2005). Solid lines are fits to the thermodynamic model (Eq. 25). The short-dashed line shows the temperature trend calculated from the 1-bar free energy of the pure components of the system (Barin et al., 1989). b) The logarithmic value of the exchange coefficient K of silicon minus the logarithmic value of the activity coefficient of Si in the metal plotted as a function of inverse temperature (10,000/T) and for different pressures as indicated.

study and literature), and lines representing the best fits. An increase of K_{Si} with pressure is predicted by the model. The pressure coefficient (c) is positive and much larger than the one (45 ± 24) obtained previously by Wade and Wood (2005). This result is also in marked contrast with the value derived by Corgne et al. (2008), who found a weak negative dependence (-11 ± 24) and the more negative dependence derived by Mann et al. (2009). This difference is not due to the experimental measurements themselves (which are actually incorporated in our multivariate regression), but to one specific hypothesis in the modelling. In contrast to the studies cited above, we did not estimate the b parameter using 1 bar free energy data. Rather,

we regressed this coefficient as a free parameter like the other coefficients (a, c, d) from the experimental data. With this approach, we derived a temperature dependence much weaker than previously reported with b being about half of previous estimates (Fig. 4a). Parameters b and c being intercorrelated, a lower value for b has led to a higher value for c. Our decision not to use the free energy data was motivated by the fact that other components, than the pure components listed in reaction (18) could influence the properties of silicate melts. Using well-constrained temperature series, the experimental study of Siebert et al. (2011) recently argued against the use of free-energy data.

The model extrapolation shows that even if K_{Si} increases with pressure and temperature, the silicon content in the metal decreases above ~45 GPa with increasing temperature because of a strong effect of the silicon activity coefficient. This effect is illustrated in Fig. 4b, where log K_{Si} — log γ_{Si} is plotted as a function of temperature. At pressure below 40 GPa, log K_{Si} — log γ_{Si} increases with increasing temperature indicating that the Si content in the metal increases with temperature. Above 50 GPa, log K_{Si} — log γ_{Si} decreases with increasing temperature, indicating a decrease in Si solubility in the metal with temperature. Whether this effect is real or just an artefact of the extrapolations is not clear. Experiments in the laser-heated DAC should shed some light into this interesting observation. Campbell et al. (2009) studied the evolution of the Ni–NiO and Fe–FeO buffers with pressure and showed a negative effect on the partition coefficient of nickel with pressure. This was explained by the crossing (or intersection) of the two buffers with pressure. In this sense, our extrapolation indicates that the Fe–FeO and Si–SiO$_2$ buffers may undergo a similar change at high pressure as suggested in Malavergne et al. (2004), but experimental confirmation is needed.

3.5. Si and O partitioning models

We estimated the multivariate standard deviation of the oxygen and silicon partition coefficients using a Monte Carlo method. Ten thousand sets of the regression coefficients were randomly picked within their respective error bars, and corresponding values of K_{Si} and K_O were calculated. We obtained a standard deviation of 0.5 for log K_{Si} and 0.4 for log K_O. To illustrate the quality of the derived parameterisations, the experimental data used in this study are plotted in a measured versus calculated plot in Fig. 5, along with the standard deviation of the regression where we can see that log K calculated with our model is in good agreement with the one obtained experimentally, within the error.

We can now use the thermodynamic model to extrapolate or interpolate the partitioning of Si and O between metal and silicate melts at different pressure, temperature and oxygen fugacity conditions. Fig. 6 shows the Si and O content in the metal calculated (for various pressures) at 3000 K as a function of the mole fraction of FeO in the silicate melt (x_{FeO}), which is the main parameter that controls oxygen fugacity. To date, there are no data on partitioning of Si and O between metal and silicate melts at pressures higher than ~25 GPa. However, a few studies were performed on molten iron and crystallised ferropericlase or perovskite in diamond anvil cell (DAC) (Frost et al., 2010; Ozawa et al., 2008; Takafuji et al., 2005). We can compare these partition coefficients with our extrapolations, shown in Fig. 6. In the case of metal–ferropericlase equilibrium, the predicted oxygen content in the metal from our model is close to results of the DAC experiments in some cases but not so much when we compare with the data obtained in multi-anvil apparatus from Asahara et al. (2007). Nevertheless, since the thermodynamical properties of the system iron melt–ferropericlase are not the same as in the system of iron-silicate melts (mainly because of the difference in the γ_{FeO} in the two oxides), we cannot predict oxygen content in other systems. For metal–perovskite equilibrium, the results from Takafuji et al. (2005) show systematically a lower Si content and a higher O content in the metal comparing to the
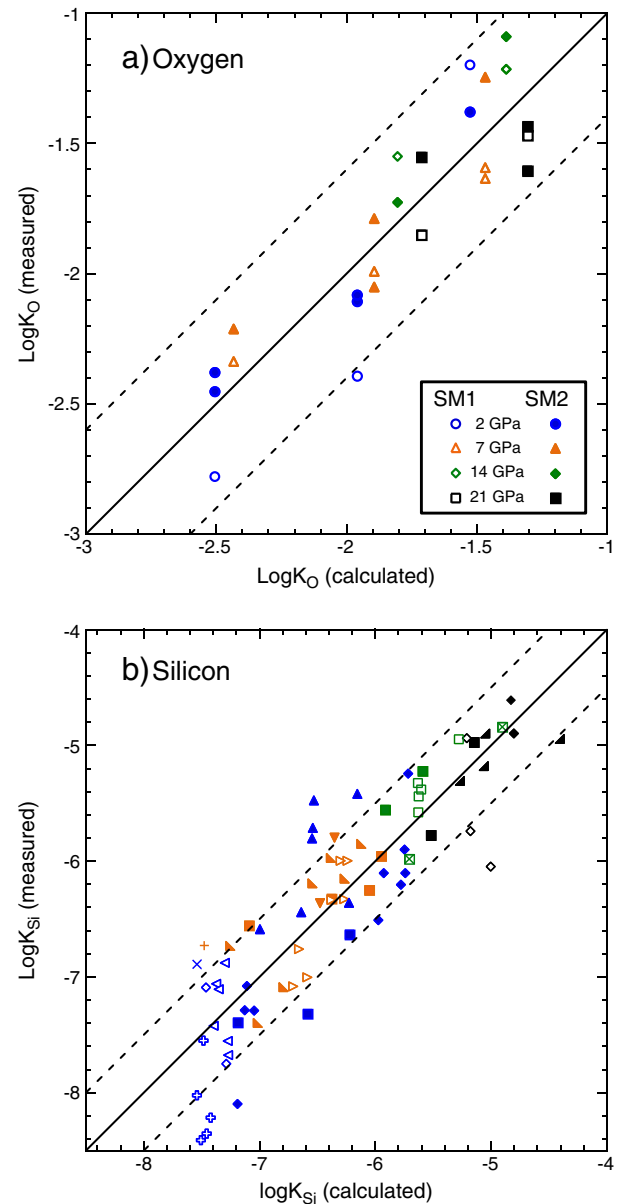

Fig. 5. Comparison between calculated and measured values of log K for oxygen (a) and silicon (b). Dashed lines are ±1σ error on the regressions. Symbols as in Fig. 4.

model predictions. These discrepancies may be due to the fact that Si and O were not buffered by another phase in the DAC experiments. In the case where metal coexist solely with silicate perovskite, there is no interplay between Si and O, and ferropericlase cannot bring the additional degree of freedom.

4. Core formation

4.1. Single stage core formation

Single stage core formation is a first order model, which could represent the average of a range of equilibrium conditions rather than just a single event. Experimental studies on the partitioning of nickel and cobalt at high pressure and high temperature have suggested the single-stage equilibrium occurred at pressure between 25 and 60 GPa and temperature between 2500 and 4000 K (e.g., Chabot et al., 2005; Gessmann et al., 2001; Li and Agee, 2001; Righter et al., 1997). However, it is not possible to explain the observed concentrations of other siderophile elements in the mantle (such as vanadium or niobium)
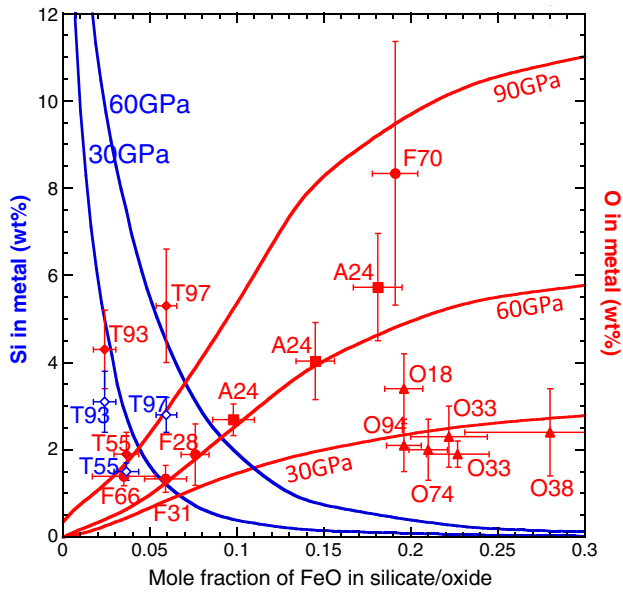
Fig. 6. Modelled Si (blue) and O (red) contents in the metal at 3000 K and 30, 60 and 90 GPa as a function of mole fraction of FeO in silicate melts. Data points are diamond anvil cell metal–mineral partitioning data from the literature. T: Takafuji et al. (2005) metal–perovskite; O: Ozawa et al. (2008) metal–ferropericlase; F: Frost et al. (2010) metal–ferropericlase; A: Asahara et al. (2007) metal–ferropericlase (multi-anvil experiments). Numbers next to letters refer to the experimental pressures. Run temperatures were around 3000 K ± 150 K in these experiments, except in Frost et al. (2010) where temperature were 2800 K at 28 and 31 GPa, 3100 K at 66 GPa and 3500 K at 70 GPa.

using single stage core formation because, to match their mantle depletion, temperature conditions would be several hundreds of degrees above the mantle liquidus (Wade and Wood, 2005). Recently, Corgne et al. (2009) proposed that the addition of about 2 to 5 wt.% oxygen in the core could explain the present-day mantle-concentration of most siderophile elements (among which V and Nb) with core equilibration occurring at approximately 40 GPa and 3200 K. The parameterisation developed in section 3 allows us to estimate the Si and O contents of the core for such a single-stage core-formation model. We used the following parameters for a peridotitic silicate melt composition: $X_{SiO2} = 0.39$, FeO = 8 wt.% ($X_{FeO} = 0.06$) and nbo/t = 2.76. Fig. 7 shows the concentrations of oxygen and silicon in the core for different magma ocean depths (i.e. basal pressures) with temperature conditions fixed on the peridotite liquidus as given in Wood et al. (2008). For equilibration conditions of about 40 GPa and 3200 K, we obtain core concentrations of 1 to 3.5 wt.% Si and 0.5 to 2.5 wt.% O. Thus, only the upper bound of this model could satisfy the oxygen content requirement to explain V and Nb partitioning in a single stage model (Corgne et al., 2009).

4.2. Continuous core formation

Continuous core formation models were recently proposed to take account of the likely progressive proto-core growth during Earth's accretion, as supported by dynamical simulations (Kaula, 1995; O'Brien et al., 2006). The core would thus be the result of multistage equilibration with increasing conditions of pressure, temperature and oxygen fugacity (Galimov, 2005; Wade and Wood, 2005). Using our thermodynamic parameterisations, we can predict the variations of the silicon and oxygen content in the metal under these varying conditions, and obtain an integral core composition along any given P–T–fO₂ path. In all the models presented below, we assumed that the Earth accreted in 1% steps (discretisation). As undertaken by Corgne et al. (2008) to match the mantle abundances of siderophile elements, the equilibration pressure at the bottom of the magma ocean
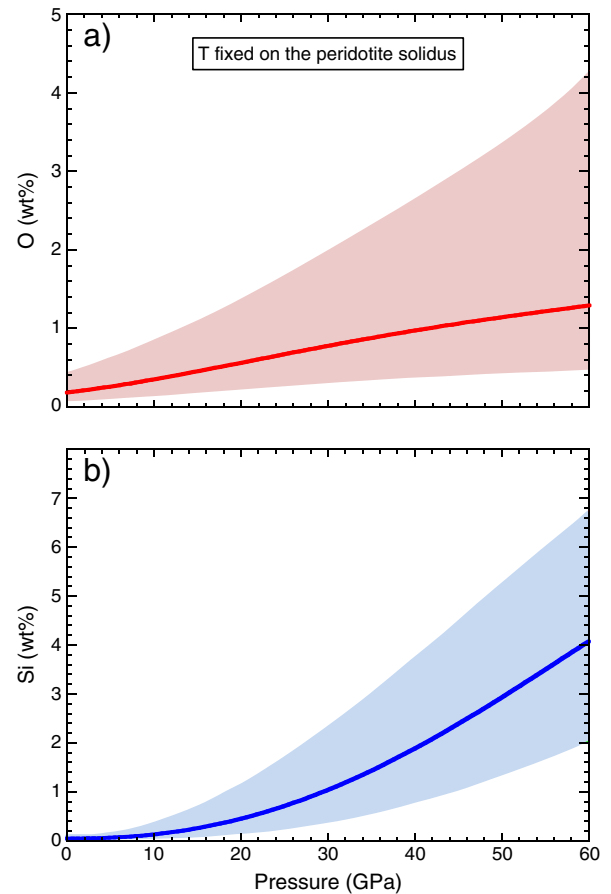

Fig. 7. Modelled oxygen (a) and silicon (b) concentrations in the metal as a function of pressure, for temperature on the peridotite liquidus. The metal is in equilibrium with a peridotite melt containing 8 wt.% FeO ($X_{FeO} = 0.06$), at an oxygen fugacity of IW-2.4. Shaded area represents 1 standard deviation uncertainty estimated using Monte-Carlo simulations (see text).

was fixed at 40% of the value of the core-mantle boundary in the proto-Earth (which gives a final magma ocean pressure of 54 GPa). We also assumed that the core constitutes 32.5 wt.% (present-day value) of the growing Earth at all times. The silicate composition is that of peridotite with $X_{SiO2} = 0.39$ and nbo/t = 2.76. We modelled four cases of continuous accretion (model (a) to (d)), corresponding to four different fO₂ paths. Fig. 8 illustrates the variations of core Si and O contents as a function of the accreted mass fraction for the four models.

Model (a) considers that oxygen fugacity remained constant during accretion (FeO = 8 wt.%, or $X_{FeO} = 0.06$ in peridotite, IW-2.4). This leads to Si and O concentrations in the core on the order of those obtained in a single-stage core-formation model at 35 GPa, yielding about 1.5 wt.% Si and 1 wt.% O (Fig. 8a).

In model (b), conditions are initially reduced (IW-4.5) and fO₂ increases continuously as the Earth accreted, from IW-4.5 to IW-2.4 at the end of accretion ($X_{FeO} = 0.006$ to 0.06 in peridotite). This model assumes an evolution of the oxidation state of the mantle by reducing SiO₂ to Si incorporated into the core and oxidising the surrounding silicate (Galimov, 2005; Javoy, 1995; O'Neill, 1991). In this case, silicon content ranges from 1.5 to 6 wt.%, and oxygen, from 0.2 to 1.3 wt.% (Fig. 8b).

A second variable fO₂ model (c), similar to that envisaged by Wade and Wood (2005), considers constant reduced conditions (IW-4.5) up to the point where the proto-Earth is large enough to have a magma ocean depth in the perovskite stability field (i.e. about 23 GPa corresponding to 30% mass accreted). This first step is followed by a continuous increase up to IW-2.4 at the end of the
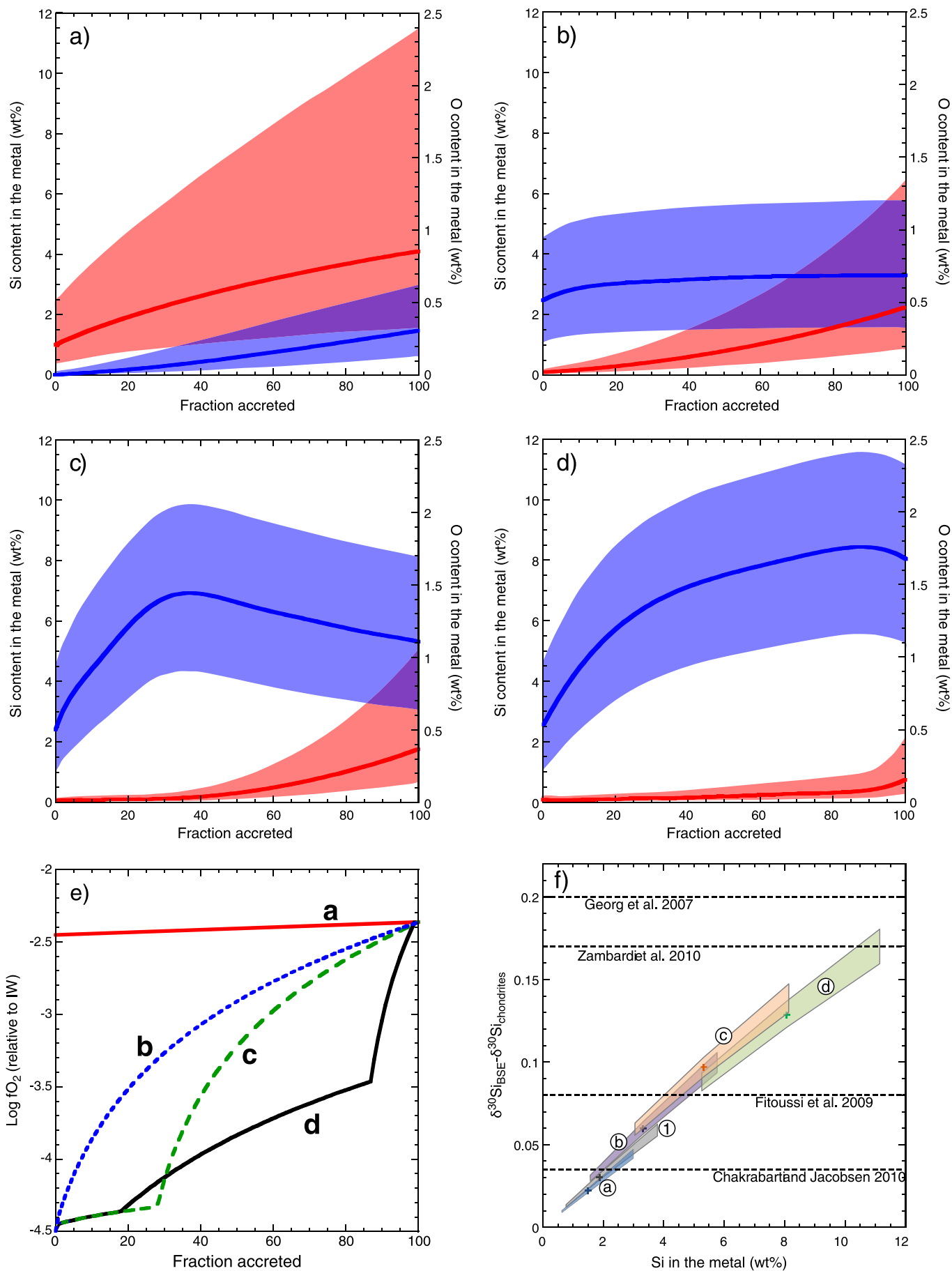
accretion ($X_{FeO} = 0.006$ to 0.06 in peridotite). This model predicts relatively low oxygen contents between 0.1 and 1.1 wt.%, and high silicon contents, between 3 and 8 wt.% (Fig. 8c).

A final variable fO₂ model (d) considers three oxygen fugacity stages, starting at IW-4.5 up to 20% accreted fraction, followed by a stepwise increases between 20% and 90% accreted fractions ($X_{FeO} = 0.006$ to 0.016 in peridotite), and a final gradual increase to IW-2.4 at the end of accretion. This model is the favoured model in Wood et al. (2008). Our calculations indicate that, in this model, silicon would be the main contributor to the light element budget in the core, ranging from 5 to 11 wt.%. Oxygen concentrations would be low, less than 0.5 wt.% (Fig. 8d).

0.73 wt.% O or 1.6 wt.% Si is needed to produce 1% density deficit according to Poirier (1994) and Chen et al. (2007). According to a density deficit between 2.9 and 7% (Anderson and Isaak, 2002), all models fit the CDD, except if we consider the lower bounds of the constant oxygen fugacity models, i.e. single stage model and continuous accretion model with constant redox conditions, which only sums up to about 1% the CDD. In the more reduced accretion models, a large amount of silicon is predicted to enter the core while oxygen content remains fairly low (Fig. 8b, c, d). For models (c) and (d), the amount of silicon alone in the metal at the end of accretion is sufficient to account for the core-density deficit. Results from Antonangeli et al. (2010) suggest a maximum Si content in the inner core of 2 wt.% to be consistent with the seismological observations. Considering the partitioning of silicon between liquid and solid iron calculated by Alfè et al. (2002), Antonangeli et al. (2010) concluded to a maximum of 4 wt.% Si in the core. This is within the range of Si content in the core calculated from models under moderately reduced conditions. However, silicon as the sole major light element may not be able to explain the density difference between the inner- and outer-core, because silicon has been suggested to partition equally between solid and liquid iron (Alfè et al., 2002; Kuwayama and Hirose, 2004). An element, which partitions preferentially in liquid metal (such as oxygen), would then be needed to match the inner-outer core density differences and seismic sound velocities (Badro et al., 2007).

4.3. Core segregation model constrained by Si isotope fractionation

Recent high-precision Si isotopic measurements have suggested that the composition of the bulk silicate Earth (BSE) differs from that of carbonaceous chondrites, with differences varying between 0.2 ± 0.1‰ and 0.035 ± 0.035‰ in $\delta^{30}Si$ notation (e.g., Chakrabarti and Jacobsen, 2010; Fitoussi et al., 2009; Georg et al., 2007; Zambardi et al., 2011). Shahar et al. (2009) showed that isotopic fractionation of silicon could occur in equilibrium between metals and silicates, implying Si isotope fractionation during core formation. The extent of fractionation between the BSE and bulk earth (BE, considered equivalent to carbonaceous chondrites) as a function of silicon entering the core can be estimated by mass balance (e.g. Chakrabarti and Jacobsen, 2010) as follows:

$$\delta^{30}Si_{BSE} - \delta^{30}Si_{bulk\ earth} = C_{core}\gamma\Delta^{30}Si_{silicate-metal}/[C_{BSE}(1-\gamma) + C_{core}\gamma] \quad (27)$$

where $\Delta^{30}Si_{silicate-metal} = 7.64 \times 10^6/T^2$ is the temperature dependence of the isotopic fractionation between metal and silicate (Ziegler et al., 2010), C_{core} and C_{BSE} are the concentrations of silicon in the core and in

the BSE, respectively, and γ is the mass fraction of the core relative to the Earth and equals to 0.325. C_{BSE} is assumed to be 21 wt.% as in pyrolite (McDonough and Sun, 1995). C_{core} was determined for the four core segregation models discussed above. The resulting Si isotopic fractionations between BE and BSE are shown in Fig. 8f as a function of Si core content. Comparison with the $\Delta^{30}Si$ between peridotites and chondrites reported in the literature reveals that it is not possible to discriminate between the various models since all the models are consistent within uncertainties with the isotopic measurements. Definitive quantitative estimation of the Si content using isotope constraints is not possible until a consensus is reached regarding the isotope compositions of chondrites and bulk silicate Earth. Nevertheless, if we consider that the Si content of the core is rather large, only the most reducing model (model d) yields the appropriate amounts of silicon. Inversely, if the Si core content is low, then models with relatively oxidising conditions should be considered.

5. Conclusions

We have measured O and Si partitioning between molten metal and silicate melts up to pressures of 21 GPa and temperatures of 2873 K. The experiments were intended to simulate the conditions of core formation in a deep magma ocean. The experimental data were used to establish a thermodynamic model that allows us to calculate the Si and O contents in the metal as a function of pressure, temperature and oxygen fugacity. We then derived core compositions for different core-formation models. The concentrations of Si and O in the core are highly dependent upon these models.

Under fixed fO₂ conditions (at the present-day core-mantle 'equilibrium' of IW-2.4), the Si and O contents in the core for a continuous core formation model are very close to those obtained in a single-stage core formation model at about 35 GPa. Under these conditions, the amount of light elements obtained in the core is rather limited (less than 3.5 wt.% Si and 2.5 wt.% O). Under moderately reduced conditions, the continuous accretion models have no single-stage equivalent. We evaluated three models with continuous oxidation through accretion; one with oxidation starting from the beginning of the accretion, the other with oxidation starting after the magma ocean reaches the depth where perovskite becomes stable (proposed by Wade and Wood, 2005), and the favoured model from Wood et al. (2008). The first model (b) yields a Si content between 2 and 6 wt.% and an O content between 0.2 and 1.5 wt.%, whereas the second model (c) yields a Si content between 3 and 8 wt.% and an O content between 0.1 and 1.1 wt. %, and the third (d), a Si content between 5 and 11 wt.% and O content lower than 0.5 wt.%. Therefore, derived oxygen core contents remain relatively modest (<2.5 wt.%) for all the formation models investigated here. Our models are well within the range of Si contents constrained from isotope fractionation studies which range from 0 to 4 wt.%, 2–8 wt.%, 9–13 wt.%, >5 wt.% according to ΔSi values of Chakrabarti and Jacobsen (2010), Fitoussi et al. (2009), Zambardi et al. (2011), Georg et al. (2007), respectively. The total light element content derived for all models is compatible with the estimations of bulk core density deficit. However, model (d) with high Si core content may not be suitable to explain the density contrast at the ICB (e.g. Alfè et al., 2002).

It is important that future works explore a wider range of P–T($-fO_2$) conditions to refine the partitioning parameterisations obtained in this contribution. The partitioning data from the current study are limited to 21 GPa and 2873 K, requiring relatively large extrapolations to model core formation in a deep magma ocean. In addition to the statistical errors due to extrapolation, unexpected property changes such as

Fig. 8. Modelled silicon and oxygen concentrations in the core for four continuous core-formation scenarios, as a function of the accreted mass fraction of the proto-Earth. a) Constant oxygen fugacity of IW-2.4 ($X_{FeO} = 0.06$). b) Continuous increase of fO₂ from IW-4.5 to IW-2.4 (FeO in the silicate melt from $X_{FeO} = 0.006$ to $X_{FeO} = 0.06$). c) Continuous increase of fO₂ from IW-4.5 to IW-2.4 after stabilisation of perovskite at the base of the magma ocean (30% accretion). d) Continuous increase of fO₂ from IW-4.5 to IW-2.4 with two major steps at 20 and 90% of accretion. e) fO₂ variation as a function of the fraction accreted for models *a–d*. f) Difference in the $\delta^{30}Si$ of the bulk silicate Earth and carbonaceous chondrites; $\delta^{30}Si_{BSE} - \delta^{30}Si_{chondrites}$ is expressed in per mil as a function of the Si content in the core. 1 refers to a single-stage core-formation model at 40 GPa and 3200 K; *a* to *d* refer to continuous models a to d. Literature values of $\Delta^{30}Si_{BSE-chondrites}$ are shown as horizontal dashed lines: 0.20 ± 0.10‰, 0.08 ± 0.04‰, 0.035 ± 0.035‰ and 0.17 ± 0.03‰, respectively from Georg et al. (2007), Fitoussi et al. (2009), Chakrabarti and Jacobsen (2010) and Zambardi et al. (2011).

new melt properties could potentially affect partitioning behaviour beyond the P–T range of the current measurements as recently mentioned in Sanloup et al. (2011).

Acknowledgements

Appendix A. Supplementary data

Supplementary data to this article can be found online at doi:10.1016/j.epsl.2011.08.004.

References

Alfè, D., Gillan, M.J., Price, G.D., 2002. Composition and temperature of the Earth's core constrained by combining ab initio calculations and seismic data. Earth Planet. Sci. Lett. 195, 91–98.

Anderson, O.L., Isaak, D.G., 2002. Another look at the core density deficit of the Earth's outer core. Phys. Earth Planet. Inter. 131, 19–27.

Antonangeli, D., Siebert, J., Badro, J., Farber, D.L., Fiquet, G., Morard, G., Ryerson, F.J., 2010. Composition of the Earth's inner core from high-pressure sound velocity measurements in Fe–Ni–Si alloys. Earth Planet. Sci. Lett. 295, 292–296.

Asahara, Y., Frost, D.J., Rubie, D.C., 2007. Partitioning of FeO between magnesiowüstite and liquid iron at high pressures and temperatures: implications for the composition of the Earth's outer core. Earth Planet. Sci. Lett. 257, 435–449.

Badro, J., Fiquet, G., Guyot, F., Gregoryanz, E., Occelli, F., Antonangeli, D., d'Astuto, M., 2007. Effect of light elements on the sound velocities in solid iron: implications for the composition of Earth's core. Earth Planet. Sci. Lett. 254, 233–238.

Barin, I., Sauert, F., Schultze-Rhonhof, E., Sheng, W.S., 1989. Thermochemical Data of Pure Substances. Part I and Part II, CH Verlagsgesellschaft, Weinheim, Germany.

Basu, S., Lahiri, A.K., Seetharaman, S., 2008. Activity of iron oxide in steelmaking slag. Metall. Mater. Trans. B 39B, 447–456.

Bertka, C.M., Fei, Y., 1997. Mineralogy of the Martian interior up to core-mantle boundary pressures. J. Geophys. Res. 102 (B3), 5251–5264.

Birch, F., 1952. Elasticity and constitution of the Earth's interior. J. Geophys. Res. 57, 227–286.

Birch, F., 1964. Density and composition of mantle and core. J. Geophys. Res. 69 (20), 4377–4388.

Campbell, A.J., Danielson, L., Righter, K., Seagle, C.T., Wang, Y., Prakapenka, V.B., 2009. High pressure effects on the iron–iron oxide and nickel–nickel oxide oxygen fugacity buffers. Earth Planet. Sci. Lett. 286, 556–564.

Chabot, N.L., Draper, D.S., Agee, C.B., 2005. Conditions of core formation in the Earth: constraints from nickel and cobalt partitioning. Geochim. Cosmochim. Acta 69, 2141–2151.

Chakrabarti, R., Jacobsen, S.B., 2010. Silicon isotopes in the inner solar system: implications for core formation, solar nebular processes and partial melting. Geochim. Cosmochim. Acta 74, 6921–6933.

Chen, B., Gao, L., Funakoshi, K., Li, J., 2007. Thermal expansion of iron-rich alloys and implications for the Earth's core. Proc. Nat. Acad. Sci. 22, 9162–9167.

Corgne, A., Keshav, S., Fei, Y., McDonough, W.F., 2007. How much potassium is in the Earth's core? New insights from partitioning experiments. Earth Planet. Sci. Lett. 256, 567–576.

Corgne, A., Keshav, S., Wood, B.J., McDonough, W.F., Fei, Y., 2008. Metal–silicate partitioning and constraints on core composition and oxygen fugacity during Earth accretion. Geochim. Cosmochim. Acta 72, 574–589.

Corgne, A., Siebert, J., Badro, J., 2009. Oxygen as a light element: a solution to single-stage core formation. Earth Planet. Sci. Lett. 288, 108–114.

Cottrell, E., Walker, D., 2006. Constraints on core formation from Pt partitioning in mafic silicate liquids at high temperatures. Geochim. Cosmochim. Acta 70, 1565–1580.

Dasgupta, R., Walker, D., 2008. Carbon solubility in core melts in a shallow magma ocean environment and distribution of carbon between the Earth's core and the mantle. Geochim. Cosmochim. Acta 72, 4627–4641.

Dreibus, G., Palme, H., 1996. Cosmochemical constraints on the sulfur content in the Earth's core. Geochim. Cosmochim. Acta 60, 1125–1130.

Dresler, W., 1989. Ironmaking Conf. Proc. ISS-AIME, Warrendale, Pennsylvania, pp. 83–87.

Fitoussi, C., Bourdon, B., Kleine, T., Oberli, F., Reynolds, B.C., 2009. Si isotope systematics of meteorites and terrestrial peridotites : implications for Mg/Si fractionation in the solar nebula and for Si in the Earth's core. Earth Planet. Sci. Lett. 287, 77–85.

Frost, D.J., 2003. Fe²⁺–Mg partitioning between garnet, magnesiowustite, and (Mg, Fe) 2SiO4 phases of the transition zone. Am. Mineral. 88, 387–397.

Frost, D.J., Asahara, Y., Rubie, D.C., Miyajima, N., Dubrovinsky, L.S., Holzapfel, C., Ohtani, E., Miyahara, M., Sakai, T., 2010. Partitioning of oxygen between the Earth's mantle and core. J. Geophys. Res. 115, B02202. doi:10.1029/2009JB006302.

Galimov, E.M., 2005. Redox evolution of the Earth caused by multi-stage formation of its core. Earth Planet. Sci. Lett. 233, 263–276.

Georg, R.B., Halliday, A.N., Schauble, E.A., Reynolds, B.C., 2007. Silicon in the Earth's core. Nature 447. doi:10.1038/nature, 05927, 1102-1106.

Gessmann, C.K., Rubie, D., 1998. The effect of temperature on the partitioning of nickel, cobalt, manganese, chromium, and vanadium at 9 GPa and constraints on formation of the Earth's core. Geochim. Cosmochim. Acta 62, 867–882.

Gessmann, C.K., Wood, B.J., Rubie, D.C., Kilburn, M.R., 2001. Solubility of silicon in liquid metal at high pressure: implications for the composition of the Earth's core. Earth Planet. Sci. Lett. 184, 367–376.

Hillgren, V.J., Drake, M.J., Rubie, D.C., 1996. High pressure and high temperature metal–silicate partitioning of siderophile elements: the important of silicate liquid composition. Geochim. Cosmochim. Acta 60, 2257–2263.

Ito, E., Morooka, K., Ujike, O., Katsura, T., 1995. Reactions between molten iron and silicate melts at high pressure: implications for the chemical evolution of Earth's core. J. Geophys. Res. 100 (B4), 5901–5910.

Jana, D., Walker, D., 1997. The influence of silicate melt composition on distribution of siderophile elements among metal and silicate liquids. Earth Planet. Sci. Lett. 150, 463–472.

Javoy, M., 1995. The integral enstatite chondrite model of the earth. Geophys. Res. Lett. 22, 2219–2222.

Kaula, W.M., 1995. Formation of the terrestrial planets. Earth Moon Planet. 67, 1–11.

Kawazoe, T., Ohtani, E., 2006. Reaction between liquid iron and (Mg, Fe)SiO3-perovskite and solubilities of Si and O in molten iron at 27 GPa. Phys. Chem. Miner. 33, 227–234.

Kegler, Ph., Holzheid, A., Frost, D.J., Rubie, D.C., Dohmen, R., Palme, H., 2008. New Ni and Co metal–silicate partitioning data and their relevance for an early terrestrial magma ocean. Earth Planet. Sci. Lett. 268, 28–40.

Kilburn, M.R., Wood, B.J., 1997. Metal–silicate partitioning and the incompatibility of S and Si during core formation. Earth Planet. Sci. Lett. 152, 139–148.

Kuwayama, Y., Hirose, K., 2004. Phase relations in the system Fe–FeSi at 21 GPa. Am. Mineral. 89, 273–276.

Li, J., Agee, C.B., 1996. Geochemistry of mantle-core differentiation at high pressure. Nature 381, 686–689.

Li, J., Agee, C.B., 2001. Element partitioning constraints on the light element composition of the Earth's core. Geophys. Res. Lett. 28, 81–84.

Ma, Z., 2001. Thermodynamic description for concentrated metallic solutions using interaction parameters. Metall. Mater. Trans. B 32B, 87–103.

Malavergne, V., Siebert, J., Guyot, F., Gautron, L., Combes, R., Hammouda, T., Borenstajn, S., Frost, D.J., Martinez, I., 2004. Si in the core? New high pressures and high temperature experimental data. Geochim. Cosmochim. Acta 68, 4201–4211.

Malavergne, V., Tarrida, M., Combes, R., Bureau, H., Jones, J., Schwandt, C., 2007. New high-pressure and high-temperature metal/silicate partitioning of U and Pb: implication for the cores of the Earth and Mars. Geochim. Cosmochim. Acta 71, 2637–2655.

Mann, U., Frost, D.J., Rubie, D.C., 2009. Evidence for high-pressure core mantle differentiation from the metal–silicate partitioning of lithophile and weakly-siderophile elements. Geochim. Cosmochim. Acta 73, 7360–7386.

McDonough, W.F., 2003. Compositional model for the Earth's core. Treatise Geochem. 2, 547–568.

McDonough, W.F., Sun, S., 1995. The composition of the Earth. Chem. Geol. 120, 223–253.

Mysen, B.O., 1988. Structure and Properties of Silicate Melts. Elsevier, Amsterdam. 354 pp.

O'Brien, D.P., Morbidelli, A., Levison, H.F., 2006. Terrestrial planet formation with strong dynamical friction. Icarus 184, 39–58.

O'Neill, H.St.C., 1991. The origin of the Moon and the early history of the Earth — a chemical model. Part 2: the Earth. Geochim. Cosmochim. Acta 55, 1159–1172.

O'Neill, H. StC, Canil, D., Rubie, D., 1998. Oxide-metal equilibria to 2500 °C and 25 GPa: implications for core formation and the light component in the Earth's core. J. Geophys. Res. 103, 12239–12260.

Ozawa, H., Hirose, K., Mitome, M., Bando, Y., Sata, N., Ohishi, Y., 2008. Chemical equilibrium between ferropericlase and molten iron to 134 GPa and implications for iron content at the bottom of the mantle. Geophys. Res. Lett. 35, L05308. doi:10.1029/2007GL032648.

Ozawa, H., Hirose, K., Mitome, M., Bando, Y., Sata, N., Ohishi, Y., 2009. Experimental study of reaction between perovskite and molten iron to 146 GPa and implications for chemically distinct buoyant layer at the top of the core. Phys. Chem. Miner. 36, 355–363 2009.

Palme, H., Jones, A., 2003. Solar system abundances of the elements. In: Davis, M. (Ed.), Meteorites, Comets and Planets. : Treatise on Geochemistry, Volume 1. Elsevier-Pergamon, Oxford, pp. 41–62.

Poirier, J.P., 1994. Light elements in the Earth's outer core: a critical review. Phys. Earth Planet. Inter. 85, 319–337.

Righter, K., 2003. Metal–silicate partitioning of siderophile elements and core formation in the early Earth. Annu. Rev. Earth Planet. Sci. 31, 135–174.

Righter, K., Drake, M.J., Yaxley, G., 1997. Prediction of siderophile element–silicate partition coefficients to 20 GPa and 2800 °C: the effects of pressure, temperature, oxygen fugacity, and silicate and metallic melt compositions. Phys. Earth Planet. Inter. 100, 115–134.

Righter, K., Pando, K.M., Danielson, L., Lee, C., 2010. Partitioning of Mo, P and other siderophile elements (Cu, Ga, Sn, Ni, Co, Cr, Mn, V and W) between metal and silicate

melt as a function of temperature and silicate melt composition. Earth Planet. Sci. Lett. 291, 1–9.

Rubie, R.C., Gessmann, C.K., Frost, D.J., 2004. Partitioning of oxygen during core formation on the Earth and Mars. Nature 429, 58–61.

Sakai, T., Kondo, T., Ohtani, E., Terasaki, H., Endo, N., Kuba, T., Suzuki, T., Kikegawa, T., 2006. Interaction between iron and post-perovskite at core-mantle boundary and core signature in plume source region. Geophys. Res. Lett. 33, L15317. doi:10.1029/2006GL026868.

Sanloup, C., van Westrenen, W., Dasgupta, R., Maynard-Casely, H., Perrillat, J.-P., 2011. Compressibility change in iron-rich melt and implications for core formation models. Earth Planet. Sci. Lett. 306, 118–122.

Shahar, A., Ziegler, K., Young, E., Ricolleau, A., Schauble, E.A., Fei, Y., 2009. Experimentally determined Si isotope fractionation between silicate and Fe metal and implications for Earth's core formation. Earth Planet. Sci. Lett. 288, 228–234.

Shibaev, S.S., Grigorovich, K.V., 2008. Solubility of oxygen in iron-silicon melts. J. Phys. Conf. Ser. 98. doi:10.1088/1742-6596/98/3/032012.

Shibaev, S.S., Krasovskii, P.V., Grigorovitch, K.V., 2005. Solubility of oxygen in iron-silicon melts in equilibrium with silica at 1873 K. ISIJ Int. 45 (9), 1243–1247.

Siebert, J., Corgne, A., Ryerson, F.J., 2011. Systematics of metal–silicate partitioning for many siderophile elements applied to Earth's core formation. Geochim. Cosmochim. Acta. doi:10.1016/j.gca.2010.12.013.

Takafuji, N., Hirose, K., Mitome, M., Bando, Y., 2005. Solubilities of O and Si in liquid iron in equilibrium with (Mg, Fe)SiO3 perovskite and the light elements in the core. Geophys. Res. Lett. 32, L06313. doi:10.1029/2005GL022773.

The Japan Society for the promotion of Science and the 19th Committee on Steelmaking, 1988. Part 2: recommended values of activity coefficients, and interaction parameters of elements in iron alloys. Steelmaking Data Sourcebook. Gordon and Breach Science Publishers, pp. 273–297.

Wade, J., Wood, B.J., 2001. The Earth's 'missing' niobium may be in the core. Nature 409, 75–78.

Wade, J., Wood, B.J., 2005. Core formation and oxidation state of the Earth. Earth Planet. Sci. Lett. 236, 78–95.

Walter, M.J., Thibault, Y., 1995. Partitioning of tungsten and molybdenum between metallic liquid and silicate melt. Science 270, 1186–1189.

Wood, B.J., Wade, J., Kilburn, M.R., 2008. Core formation and the oxidation state of the Earth: additional constraints from Nb, V and Cr partitioning. Geochim. Cosmochim. Acta 72, 1415–1426.

Zambardi, T., Poitrasson, F., Corgne, A., Méheut, M., Quitté, G., Anand, M., 2011. Silicon isotope variations in the inner solar system: Implications for planetary formation, differentiation and composition. Submitted to Geochim. Cosmochim. Acta.

Ziegler, K., Young, E.D., Schauble, E.A., Wasson, J.T., 2010. Metal–silicate silicon isotope fractionation in enstatite meteorites and constraints on Earth's core formation. Earth Planet. Sci. Lett. 295, 487–496.